3-D induction log modelling with integral equation method and domain decomposition pre-conditioning

Saputera, D. H.; Jakobsen, M.; van Dongen, K. W.A.; Jahani, N.; Eikrem, K. S.; Alyaev, S.

DOI
10.1093/gji/ggad454

Publication date
2024

Document Version
Final published version

Published in
Geophysical Journal International

Geophysical Journal International

Geophys. J. Int. (2024) **236,** 834–848
Advance Access publication 2023 November 21
GJI Applied and Marine Geophysics

https://doi.org/10.1093/gji/ggad454

3-D induction log modelling with integral equation method and domain decomposition pre-conditioning

D.H. Saputera [1], M. Jakobsen,[1] K.W.A. van Dongen,[2] N. Jahani,[3] K.S. Eikrem [3] and S. Alyaev[3]

[1] *Department of Earth Science, University of Bergen, Bergen, Postboks* 7803, 5007*, Norway. E-mail: durra.saputera@uib.no*
[2] *Department of Imaging Physics, Delft University of Technology, Delft, P.O. Box* 5046, 2600 *GA, The Netherlands*
[3] *Energy Department, NORCE Norwegian Research Centre, Bergen, Postboks* 22, 5838*, Norway*

Accepted 2023 November 20. Received 2023 November 14; in original form 2023 June 12

SUMMARY

The deployment of electromagnetic (EM) induction tools while drilling is one of the standard routines for assisting the geosteering decision-making process. The conductivity distribution obtained through the inversion of the EM induction log can provide important information about the geological structure around the borehole. To image the 3-D geological structure in the subsurface, 3-D inversion of the EM induction log is required. Because the inversion process is mainly dependent on forward modelling, the use of a fast and accurate forward modelling tool is essential. In this paper, we present an improved version of the integral equation (IE) based modelling technique for general anisotropic media with domain decomposition pre-conditioning. The discretized IE after domain decomposition equals a fixed-point equation that is solved iteratively with either the block Gauss–Seidel or Jacobi pre-conditioning. Within each iteration, the inverse of the block matrix is computed using a Krylov subspace method instead of a direct solver. An additional reduction in computational time is obtained by using an adaptive relative residual stopping criterion in the iterative solver. Using this domain decomposition scheme, numerical experiments show computation time reductions by factors of 1.97–2.84 compared to solving the full-domain IE with a GMRES solver and a contraction IE pre-conditioner. Additionally, the reduction of memory requirement for covering a large area of the induction tool sensitivity enables acceleration with limited GPU memory. Hence, we conclude that the domain decomposition method is improving the efficiency of the IE method by reducing the computation time and memory requirement.

Key words: Electromagnetic theory; Numerical modelling; Numerical solutions.

1 INTRODUCTION

State-of-the-art tools for electromagnetic (EM) induction logging-while-drilling (LWD) enable real-time mapping of formation boundaries tens of metres away from the borehole (Sinha *et al.* 2022). These tools typically consist of multiple antenna configurations that have different sensitivities to the electrical resistivity distribution in the medium around the borehole. The distribution of the electrical properties is quantified through an inversion process and provides structural information and characteristics of the surrounding medium. The studies in real-time geosteering inversion usually employ 1-D or 2-D approximations (Pardo & Torres-Verdín 2015; Bakr *et al.* 2017; Puzyrev 2019; Noh *et al.* 2022). However, for imaging complex geological structures, it is important to capture the 3-D variability of the resistivity change around the borehole through 3-D inversion methods (Puzyrev *et al.* 2019; Sinha *et al.* 2022). The work of Wilson *et al.* (2019) shows that it is possible to perform 3-D inversion in real-time, however, it is challenging due to the large computational cost required for the 3-D forward modelling, especially when quantification of the uncertainties in the inversion is required. Therefore, the study of a fast 3-D forward solver that accurately models induction logs remains essential for the development and testing of new imaging methods.

The integral equation (IE) method is one of the most widely applied numerical methods for the 3-D modelling of EM data (Avdeev 2005; Wang *et al.* 2021) alongside the finite-difference (Newman & Alumbaugh 2002; Hou *et al.* 2006) and finite-element methods (Puzyrev *et al.* 2013; Ren *et al.* 2014). One of the main advantages of using the IE method is that it has the accuracy of a semi-analytical solution (Wang *et al.* 2021). Without introducing many specific approximations, the EM fields around the borehole are obtained by solving the linear system arising from the discretization of the IEs. As the linear system is dense, the computational memory and time required can be large compared to other

numerical methods (Zaslavsky *et al.* 2011; Yoon *et al.* 2016). To overcome this challenge, the linear system can be efficiently solved using an iterative solver based on the Krylov subspace method in combination with the utilization of FFTs (Fast Fourier Transform) to accelerate the convolution integral operations in the linear system (Fang *et al.* 2006). A faster convergence rate can be achieved by implementing the contraction IE formulation (Hursan & Zhdanov 2002) which works especially well in the presence of a high contrast or a high degree of anisotropy. Additionally, the application of GPUs further decreases computation times because GPUs enable the acceleration of mathematical operations that can be straightforwardly parallelized (Dyatlov *et al.* 2015; Saputera *et al.* 2022).

In the work of Zhdanov *et al.* (2006), the formulation of the IE method is extended by decomposing the region of interest into several subdomains. The field in the entire domain is obtained by sequentially solving the linear system in each subdomain and updating the interaction between the subdomains iteratively until convergence. With this formulation, it becomes feasible to conduct large-scale modelling of surface EM data in heterogeneous media as the computational operation can be reduced to one subdomain at a time. It is possible to obtain an additional reduction in computational costs by only considering subdomains that contain an anomaly with respect to the background medium. This leads to a smaller number of discretization blocks required for the 3-D modelling while still enabling FFT implementation (Endo *et al.* 2009) and an improved iterative solver convergence rate (Van Dongen *et al.* 2007). Typically, a horizontally layered model is chosen as the background medium as the theory of Green's functions for layered 1-D models is very well developed (Zhdanov *et al.* 2006). Hence, the IE method can be very efficient when the resistivity model only deviates in some areas from the 1-D model. However, in our application, the subsurface structure can vary in all directions. The subdomains containing an anomaly can be everywhere around the EM tools and it may not be possible to achieve a reduction in the number of discretizations by the domain decomposition. Additionally, the subdomains from the decomposition can be adjacent to each other such that the interactions between neighbouring subdomains are not negligible.

The domain decomposition method can lead to an efficient way of solving the linear system of the IE method (Jakobsen & Tveit 2018; Wang *et al.* 2017). In the work of Jakobsen & Tveit (2018), the domain decomposition method is used to efficiently compute the *T*-matrix for the inversion of controlled source EM data. It is also shown that the domain decomposition method opens up the possibility to compute the *T*-matrix in parallel.

In this paper, we demonstrate that the formulation of an IE with domain decomposition (IE-DD) can be interpreted as a preconditioned linear system, offering a computational advantage. We illustrate that the IE-DD method can be represented as a fixed-point equation, which is iteratively solved using block Gauss–Seidel or Jacobi pre-conditioners (Saad 2003). In particular, we will use a Krylov subspace method to invert the block matrices that are present in the formulation. Instead of expressing the decomposition formulation in terms of the contrast source in each subdomain as described in Zhdanov *et al.* (2006) and Endo *et al.* (2009), we present the domain decomposition formulation in terms of the electric field in each sub-domain and a different perspective on the derivation of the IE-DD formulation. Additionally, we propose the use of an inexact iterative solver when solving the IE linear system for each subdomain where the target tolerance is adapted based on the full-domain residual.

The outline of this paper is described as follows. In Section 2 called theory, we give an overview of the theory and implementation of the conventional IE method and the IE-DD. In Section 3 called numerical results and discussion, we present three numerical examples to show the performance of the IE-DD method and discuss the computational aspect of our implementation. First, we show an example with isolated subdomains to verify if the domain decomposition formulation will produce the same numerical results as the conventional full-domain formulation. Also, we show different IE-DD schemes and compare the performance of these schemes with each other and the full-domain IE as a reference. In the second example, we show a numerical experiment with a simple anisotropic faulted medium to demonstrate the benefit of using IE-DD in the case of connected subdomains. In the last example, we simulate a logging scenario across a large complex 3-D model. Furthermore, we showcase the ability of the domain decomposition method to reduce the memory requirement for dealing with a large number of grid blocks in the last example. This feature lets us cover more portion of the subsurface receivers while keeping a fine grid size, which may not be straightforward to implement in our currently available computer without the domain decomposition method. In Section 4, we provide a compact evaluation of the IE-DD implementation in this study and also some possible improvements for future research. This paper contains appendices with more in-depth details of the IE-DD derivation and implementation. We also include the comparison of our conventional IE code and existing code as a benchmark of our work in Appendix B.

2 THEORY

2.1 The integral equation method for 3-D induction logs modelling

Maxwell's equations for heterogeneous media (Wannamaker & Zhdanov 2002) are the basic theory for modelling the induction tools' response within the frequency domain:

$$\nabla \times s\boldsymbol{E}(\boldsymbol{r}) = i\omega\mu\boldsymbol{H}(\boldsymbol{r}) + \boldsymbol{J}^{H}(\boldsymbol{r}), \tag{1}$$

$$\nabla \times \boldsymbol{H}(\boldsymbol{r}) = \widehat{\boldsymbol{\sigma}}(\boldsymbol{r})\boldsymbol{E}(\boldsymbol{r}), \tag{2}$$

where $\boldsymbol{E}(\boldsymbol{r})$ and $\boldsymbol{H}(\boldsymbol{r})$ are the total electric and magnetic fields, respectively, at location $\boldsymbol{r}$, $\boldsymbol{J}^{H}(\boldsymbol{r})$ denotes the magnetic source term, ω is the angular frequency, μ is the magnetic permeability, $\widehat{\boldsymbol{\sigma}}(\boldsymbol{r}) = \boldsymbol{\sigma}(\boldsymbol{r}) - i\omega\boldsymbol{\varepsilon}(\boldsymbol{r})$ is the complex electric conductivity, $\boldsymbol{\varepsilon}$ is the dielectric permittivity and $i = \sqrt{-1}$. We assume that the magnetic permeability is constant and it is set equal to the magnetic permeability of the vacuum μ_0. Additionally, the imaginary part of the complex conductivity can be ignored in the diffusion regime, which is a typical assumption for the operating conditions of induction tools.

The total electric and magnetic fields can be formulated using the following IEs (Fang *et al.* 2006)

$$\boldsymbol{E}(\boldsymbol{r}) = \boldsymbol{E}^{(0)}(\boldsymbol{r}) + \int_{\Omega} \boldsymbol{G}^{E}(\boldsymbol{r},\boldsymbol{r}')\Delta\boldsymbol{\sigma}(\boldsymbol{r}')\boldsymbol{E}(\boldsymbol{r}')\,\mathrm{d}V(\boldsymbol{r}'), \tag{3}$$

$$\boldsymbol{H}(\boldsymbol{r}) = \boldsymbol{H}^{(0)}(\boldsymbol{r}) + \int_{\Omega} \boldsymbol{G}^{H}(\boldsymbol{r},\boldsymbol{r}')\Delta\boldsymbol{\sigma}(\boldsymbol{r}')\boldsymbol{E}(\boldsymbol{r}')\,\mathrm{d}V(\boldsymbol{r}'), \tag{4}$$

where the Ω indicates the domain of integration where anomalies in the conductivity relative to the homogeneneous isotropic background conductivity σ_0 are present. The integral terms in eqs (3) and (4) represent the scattered electric and magnetic fields, respectively, due to the presence of these anomalies. The (0) superscripts indicate

the fields defined for the background medium which are referred to as the background fields. We choose a homogeneous isotropic background medium for simplicity and efficiency when calculating Green's tensor (Fang *et al.* 2006), and we assume that the tool is not always surrounded by a horizontally layered medium. The tensor $\Delta\boldsymbol{\sigma}(\boldsymbol{r}) = \boldsymbol{\sigma}(\boldsymbol{r}) - \sigma_0 \boldsymbol{I}$, denotes the conductivity contrast between the actual anisotropic and the background medium, and with $\boldsymbol{I}$ the identity tensor. The electric Green's tensor $\boldsymbol{G}^E(\boldsymbol{r}, \boldsymbol{r'})$ and its relation to the magnetic Green's tensor $\boldsymbol{G}^H(\boldsymbol{r}, \boldsymbol{r'})$ for a homogenous isotropic medium are (Fang *et al.* 2006)

$$\boldsymbol{G}^E(\boldsymbol{r}, \boldsymbol{r'}) = \left(i\omega\mu_0 \boldsymbol{I} + \frac{\nabla\nabla}{\sigma_0}\right) g(\boldsymbol{r}, \boldsymbol{r'}), \tag{5}$$

$$\boldsymbol{G}^H(\boldsymbol{r}, \boldsymbol{r'}) = (i\omega\mu_0)^{-1} \nabla \times \boldsymbol{G}^E, \tag{6}$$

$$g(\boldsymbol{r}, \boldsymbol{r'}) = \frac{e^{ik_0|\boldsymbol{r}-\boldsymbol{r'}|}}{4\pi|\boldsymbol{r}-\boldsymbol{r'}|}, \tag{7}$$

where $g(\boldsymbol{r}, \boldsymbol{r'})$ is the scalar Green's function and $k_0 = \sqrt{i\omega\mu_0\sigma_0}$. To calculate the total magnetic fields, the total electric fields need to be obtained first by solving eq. (3). Afterward, the calculation of the total magnetic fields is a straightforward addition of the background magnetic fields and the integral term as shown in eq. (4). Therefore, the main computational challenge of the IE method is to solve integral eq. (3), which is classified as a Fredholm IE of the second kind (Fang *et al.* 2006).

2.2 Numerical implementation of the integral equation method

A numerical solution of the volume integral in eq. (3) can be obtained using the method of moments (Gibson 2021). The subsurface model around the induction tool is discretized into a set of cubic grid blocks with centroids $\boldsymbol{r}^j$ and volume of Δv, where j indicates the jth grid block. The discretization of eq. (3) leads to a linear system of equations that can be expressed in operator form as

$$(\boldsymbol{I} - \boldsymbol{\mathcal{G}}\Delta\boldsymbol{\sigma})\boldsymbol{E} = \boldsymbol{E}^{(0)}, \tag{8}$$

where $\boldsymbol{\mathcal{G}}$ is the operator that represents the discrete convolution integral of the electric Green's tensor $\boldsymbol{G}^E(\boldsymbol{r}, \boldsymbol{r'})$ with the contrast source $\Delta\boldsymbol{\sigma}\boldsymbol{E}$ in eq. (3). For discretization with cubic grid blocks, the Green's function in eq. (5) can be discretized by separating the non-singular part of the Green's function and dealing with the singularity by integrating the Green's function of a grid block over a spherical domain with an equivalent volume (Gao *et al.* 2005; Jakobsen & Tveit 2018). The linear system in eq. (8) can be efficiently solved using a Krylov subspace method because it does not require the matrix of the linear system to be formed explicitly. The desired accuracy of the iterative method is quantified by the relative residual ϵ which is calculated as

$$\epsilon = \frac{\left\|\boldsymbol{E}^{(0)} - (\boldsymbol{I} - \boldsymbol{\mathcal{G}}\Delta\boldsymbol{\sigma})\boldsymbol{E}\right\|}{\left\|\boldsymbol{E}^{(0)}\right\|}, \tag{9}$$

where $\|\cdot\|$ is the L_2-norm. In this study, we use the generalized minimum residual or GMRES (Saad & Schultz 1986) as the linear system solver.

Green's tensor operator exhibits a convolution structure in each of the tensor components. This property enables the use of FFT to convolve a Green's tensor component G^E_{pq} and a component of the contrast source $(\Delta\boldsymbol{\sigma}\boldsymbol{E})_q$ efficiently (Fang *et al.* 2006). The p and q indices indicate the component of Green's tensor and the contrast source vector with p and $q = x, y, z$. At each step of the iterative solver, the convolution integral can be efficiently calculated by

$$\mathcal{G}_{pq}(\Delta\boldsymbol{\sigma}\boldsymbol{E})_q = \mathcal{F}^{-1}\left(\mathcal{F}\left[G^E_{pq}\right] \odot \mathcal{F}\left[(\Delta\boldsymbol{\sigma}\boldsymbol{E})_q\right]\right), \tag{10}$$

where $\mathcal{F}$ is the FFT operator and $\odot$ denotes elementwise multiplication. This operation reduces the convolution computation complexity from $O(N^2)$ to $O(N\log^2 N)$ with N the number of grid blocks. It should be noted that the FFT convolution requires uniform grid discretization. Although there exist several studies that employ FFT convolution on non-uniform grid settings (Nie *et al.* 2013; Kamm & Pedersen 2014; Chen *et al.* 2021), we keep a uniform grid discretization in this paper and the usage of non-uniform grid discretization with domain decomposition is subject to future study. Additionally, the size of the discretized contrast source $\Delta\boldsymbol{\sigma}\boldsymbol{E}$ needs to be padded by zeros such that the padded $\Delta\boldsymbol{\sigma}\boldsymbol{E}$ has twice the original number of points in all directions to avoid the periodicity in the FFT convolution result. The FFT of Green's tensor can be pre-calculated before calling the iterative solvers to save computational time during the iterative process.

The convergence of the Krylov solver can be improved using the pre-conditioning introduced in the contraction IE method (Hursan & Zhdanov 2002). In the contraction IE method, eq. (8) is pre-conditioned by multiplying both sides of the equation with $\sqrt{Re\sigma_0}$ and solving for the scaled electric field $(\boldsymbol{a}\boldsymbol{E})$ instead of the electric field $\boldsymbol{E}$ which results in the following:

$$\sqrt{Re\sigma_0}(\boldsymbol{I} - \boldsymbol{\mathcal{G}}\Delta\boldsymbol{\sigma})\boldsymbol{a}^{-1}(\boldsymbol{a}\boldsymbol{E}) = \sqrt{Re\sigma_0}\boldsymbol{E}^0, \tag{11}$$

where

$$\boldsymbol{a} = \frac{2Re\sigma_0\boldsymbol{I} + \Delta\boldsymbol{\sigma}^{(i)}}{\left(2\sqrt{Re\sigma_0}\right)}. \tag{12}$$

2.3 Domain decomposition

The domain decomposition method attempts to solve the problem for the entire from solutions of the different subdomains (Saad 2003). In our case, the spatial domain Ω is decomposed into M non-overlapping rectangular subdomains Ω_j, hence

$$\Omega = \bigcup_{j=1}^{M} \Omega_j, \tag{13}$$

see Fig. 1. Adapting the domain decomposition formulation described in Endo *et al.* (2009), the convolution integral term or the scattered electric field term in eq. (3) can be expressed as a sum of scattered electric fields from each of the subdomains. Subsequently,

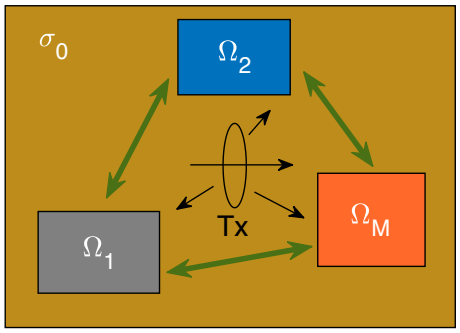

Figure 1. Schematic of the domain decomposition. The black arrows indicate the field coming from the transmitter Tx to the subdomains Ω_j. The double-headed green arrows indicate the scatterers' interaction between the subdomains. The transmitter can also be located in the anomalous domain.

eq. (3) can be written as

$$\boldsymbol{E}(\boldsymbol{r}) = \boldsymbol{E}^{(0)}(\boldsymbol{r}) + \sum_{j=1}^{M} \int_{\Omega_j} \boldsymbol{G}^{E}(\boldsymbol{r}, \boldsymbol{r}')\, \Delta\boldsymbol{\sigma}(\boldsymbol{r}')\, \boldsymbol{E}(\boldsymbol{r}')\, \mathrm{d}V(\boldsymbol{r}'), \quad (14)$$

where Ω_j indicates the subdomains with the conductivity anomaly. From eq. (14), we obtain the following set of IEs evaluated in each subdomain:

$$\boldsymbol{E}^{(i)} = \boldsymbol{E}^{(i,0)} + \sum_{j=1}^{M} \mathcal{G}^{(ij)} \Delta\boldsymbol{\sigma}^{(j)} \boldsymbol{E}^{(j)}, \quad i = 1, 2, \ldots, M. \quad (15)$$

The terms $\boldsymbol{E}^{(i,0)}$, $\boldsymbol{E}^{(i)}$ and $\Delta\boldsymbol{\sigma}^{(i)}$ are the background electric field, total electric field and the conductivity contrast defined at the subdomain Ω_i, respectively. The terms $\mathcal{G}^{(ij)}\Delta\boldsymbol{\sigma}^{(j)}\boldsymbol{E}^{(j)}$ in eq. (15) are the discrete representations of the convolution integral in eq. (14) which denote the scattered electric fields in the subdomain Ω_i due to the contrast source in the subdomain Ω_j. It can be seen in eq. (15) that the region without a conductivity anomaly does not contribute to the sum and hence can be omitted from the discretization when calculating the electric field. By collecting the scattered field terms into the left-hand side of the equations, the linear system of equations in eq. (15) can be expressed with a block-matrix representation, viz.

$$\boldsymbol{A}\widetilde{\boldsymbol{E}} = \widetilde{\boldsymbol{E}}^{(0)}, \quad (16)$$

where $\boldsymbol{A}$ is the block matrix of the re-arranged linear system according to the domain decomposition

$$\boldsymbol{A} = \begin{bmatrix} \boldsymbol{I} - \mathcal{G}^{(11)}\Delta\boldsymbol{\sigma}^{(1)} & -\mathcal{G}^{(12)}\Delta\boldsymbol{\sigma}^{(2)} & \ldots & -\mathcal{G}^{(1M)}\Delta\boldsymbol{\sigma}^{(M)} \\ -\mathcal{G}^{(21)}\Delta\boldsymbol{\sigma}^{(1)} & \boldsymbol{I} - \mathcal{G}^{(22)}\Delta\boldsymbol{\sigma}^{(2)} & \ldots & -\mathcal{G}^{(2M)}\Delta\boldsymbol{\sigma}^{(M)} \\ \vdots & \vdots & \ddots & \vdots \\ -\mathcal{G}^{(M1)}\Delta\boldsymbol{\sigma}^{(1)} & -\mathcal{G}^{(M2)}\Delta\boldsymbol{\sigma}^{(2)} & \ldots & \boldsymbol{I} - \mathcal{G}^{(MM)}\Delta\boldsymbol{\sigma}^{(M)} \end{bmatrix}, \quad (17)$$

where $\widetilde{\boldsymbol{E}}$ and $\widetilde{\boldsymbol{E}}^{(0)}$ are the block vectors containing the total and background electric fields in different subdomains, respectively. These terms are defined as

$$\widetilde{\boldsymbol{E}} = \begin{bmatrix} \boldsymbol{E}^{(1)} \\ \boldsymbol{E}^{(2)} \\ \vdots \\ \boldsymbol{E}^{(M)} \end{bmatrix}, \quad \widetilde{\boldsymbol{E}}^{(0)} = \begin{bmatrix} \boldsymbol{E}^{(1,0)} \\ \boldsymbol{E}^{(2,0)} \\ \vdots \\ \boldsymbol{E}^{(M,0)} \end{bmatrix}. \quad (18)$$

Each block in the matrix $\boldsymbol{A}$ indicates interaction terms between the subdomains. The diagonal terms $\left(\boldsymbol{I} - \mathcal{G}^{(ii)}\Delta\boldsymbol{\sigma}^{(i)}\right)$ in eq. (17) can be interpreted as the intradomain interaction within a subdomain, while the off-diagonal terms $-\mathcal{G}^{(ij)}\Delta\boldsymbol{\sigma}^{(j)}$ represent the interdomain interaction terms. Since the subdomains are rectangular, the convolution integrals with Green's tensor in the intra- and interdomain interaction terms can still be calculated using the FFT.

To solve the re-arranged linear system of equation with domain decomposition in eq. (16), the matrix $\boldsymbol{A}$ is pre-conditioned by splitting the matrix into a strictly lower triangular ($\boldsymbol{L}$), strictly upper triangular ($\boldsymbol{U}$) and diagonal ($\boldsymbol{D}$) part (Barrett *et al.* 1994; Saad 2003):

$$\boldsymbol{A} = (\boldsymbol{L} + \boldsymbol{U} + \boldsymbol{D}), \quad (19)$$

where the matrices $\boldsymbol{L}$, $\boldsymbol{U}$ and $\boldsymbol{D}$ are defined by

$$\boldsymbol{L} = \begin{bmatrix} \boldsymbol{0} & \boldsymbol{0} & \ldots & \boldsymbol{0} \\ -\mathcal{G}^{(21)}\Delta\boldsymbol{\sigma}^{(1)} & \boldsymbol{0} & \ldots & \boldsymbol{0} \\ \vdots & \vdots & \ddots & \vdots \\ -\mathcal{G}^{(M1)}\Delta\boldsymbol{\sigma}^{(1)} & -\mathcal{G}^{(M2)}\Delta\boldsymbol{\sigma}^{(2)} & \ldots & \boldsymbol{0} \end{bmatrix},$$

$$\boldsymbol{U} = \begin{bmatrix} \boldsymbol{0} & -\mathcal{G}^{(12)}\Delta\boldsymbol{\sigma}^{(2)} & \ldots & -\mathcal{G}^{(1M)}\Delta\boldsymbol{\sigma}^{(M)} \\ \boldsymbol{0} & \boldsymbol{0} & \ldots & -\mathcal{G}^{(2M)}\Delta\boldsymbol{\sigma}^{(M)} \\ \vdots & \vdots & \ddots & \vdots \\ \boldsymbol{0} & \boldsymbol{0} & \ldots & \boldsymbol{0} \end{bmatrix}, \quad (20)$$

and

$$\boldsymbol{D} = \begin{bmatrix} \boldsymbol{I} - \mathcal{G}^{(11)}\Delta\boldsymbol{\sigma}^{(1)} & \boldsymbol{0} & \ldots & \boldsymbol{0} \\ \boldsymbol{0} & \boldsymbol{I} - \mathcal{G}^{(22)}\Delta\boldsymbol{\sigma}^{(2)} & \ldots & \boldsymbol{0} \\ \vdots & \vdots & \ddots & \vdots \\ \boldsymbol{0} & \boldsymbol{0} & \ldots & \boldsymbol{I} - \mathcal{G}^{(MM)}\Delta\boldsymbol{\sigma}^{(M)} \end{bmatrix},$$

respectively. By substituting the matrix splitting in eq. (19) into eq. (16) and some simple algebra, we obtain

$$\widetilde{\boldsymbol{E}} = (\boldsymbol{D} + \boldsymbol{L})^{-1}\left[\widetilde{\boldsymbol{E}}^{(0)} - \boldsymbol{U}\widetilde{\boldsymbol{E}}\right], \quad (21)$$

which can be solved by choosing an initial guess of $\widetilde{\boldsymbol{E}}$ and iteratively calculating the following

$$\widetilde{\boldsymbol{E}}^{k+1} = (\boldsymbol{D} + \boldsymbol{L})^{-1}\left[\widetilde{\boldsymbol{E}}^{(0)} - \boldsymbol{U}\widetilde{\boldsymbol{E}}^{k}\right], \quad (22)$$

with k the iteration number. The iteration described in eq. (22) corresponds to the block Gauss–Seidel iterative method (Barrett *et al.* 1994; Saad 2003). The matrix $(\boldsymbol{D} + \boldsymbol{L})$ has a lower triangular form where the inverse can be obtained using forward substitution (Venkateshan & Swaminathan 2014). The forward substitution process to compute eq. (22) is outlined in Appendix A. With the forward substitution, the total electric field update in each subdomain according to eq. (22) can be expressed in the simple form as

$$\boldsymbol{E}^{(i),k+1} = \left(\boldsymbol{I} - \mathcal{G}^{(ii)}\Delta\boldsymbol{\sigma}^{(i)}\right)^{-1}\left[\boldsymbol{E}^{(i,0)} + \sum_{j=1}^{i-1} \mathcal{G}^{(ij)}\Delta\boldsymbol{\sigma}^{(j)}\boldsymbol{E}^{(j),k+1} + \sum_{j=i+1}^{M} \mathcal{G}^{(ij)}\Delta\boldsymbol{\sigma}^{(j)}\boldsymbol{E}^{(j),k}\right], \quad (23)$$

where $i = 1,2, \ldots, M$ denotes the number of inner iterations where the IE is solved for one subdomain and the number k denotes the number of the total domain sweeps where the electric field is updated for the entire domain. The inverse operation of the block intradomain term in eq. (23) is not calculated using the direct solver, but instead by using a Krylov subspace method to solve the following linear system of equations within each subdomain:

$$\left(\boldsymbol{I} - \mathcal{G}^{(ii)}\Delta\boldsymbol{\sigma}^{(i)}\right)\boldsymbol{E}^{(i),k+1} = \boldsymbol{E}^{(i,0)} + \sum_{j=1}^{i-1} \mathcal{G}^{(ij)}\Delta\boldsymbol{\sigma}^{(j)}\boldsymbol{E}^{(j),k+1} + \sum_{j=i+1}^{M} \mathcal{G}^{(ij)}\Delta\boldsymbol{\sigma}^{(j)}\boldsymbol{E}^{(j),k}. \quad (24)$$

The domain sweep is carried out until the relative residual on the whole domain reaches a desired threshold. The resulting operation of solving eq. (24) iteratively is equivalent to the formulation described in Zhdanov *et al.* (2006) and Endo *et al.* (2009). However, in our derivation, we can see the link between the original formulation to a block-pre-conditioned iterative method, which is the block

Gauss–Seidel iterative method in this case. The convergence of the Gauss–Seidel iterative method depends on the diagonal dominance of the linear system matrix (Saad 2003). In this case, if the sum of the interdomain terms' norm is small compared to the norm of the intradomain terms in eq. (24), then this scheme is guaranteed to converge. Since the magnitude of Green's tensor elements depends on the distance between subdomains, the interaction terms are small when the subdomains are isolated from each other. When a subdomain has small contrasts, the interaction is one-sided from the subdomain with high contrast. Additionally, the domain order may affect the convergence rate of the Gauss–Seidel iterative method (Barrett *et al.* 1994) because the ordering of the subdomains determines the matrix $(\boldsymbol{D}+\boldsymbol{L})$, which controls the convergence rate. These properties should be considered when designing the domain decomposition settings.

Instead of the Gauss–Seidel iterative method, one can also choose the Jacobi iterative method by taking only the diagonal part of the matrix $\boldsymbol{A}$ as the pre-conditioner of the fixed-point equation instead of its lower triangular part. The fixed-point equation that corresponds to the Jacobi iterative method can be written as

$$\widetilde{\boldsymbol{E}}^{k+1} = \boldsymbol{D}^{-1}\left[\widetilde{\boldsymbol{E}}^{(0)} - (\boldsymbol{L}+\boldsymbol{U})\,\widetilde{\boldsymbol{E}}^{k}\right], \tag{25}$$

which leads to the following linear system of equations to be solved in each subdomain:

$$\left(\boldsymbol{I} - \boldsymbol{\mathcal{G}}^{(ii)}\Delta\boldsymbol{\sigma}^{(i)}\right)\boldsymbol{E}^{(i),k+1} = \boldsymbol{E}^{(i,0)} + \sum_{j=1}^{M}\boldsymbol{\mathcal{G}}^{(ij)}\Delta\boldsymbol{\sigma}^{(j)}\boldsymbol{E}^{(j),k}. \tag{26}$$

Since the right-hand side of eq. (26) only depends on the solutions at the kth iteration, the Jacobi iterative method is more straightforward to be implemented in parallel computing environments (Barrett *et al.* 1994). In this case, the linear system of equations at each subdomain can be solved with the Krylov solver in parallel and the interaction terms are updated after the Krylov solver computations are done for all subdomains. The main drawback is that the Gauss–Seidel method generally has better convergence properties than the Jacobi method (Barrett *et al.* 1994).

To further improve the computation speed, we propose to use a Krylov solver with adaptive target residual when solving the IE linear system of a subdomain. The main idea is that the relative residual of the Krylov solver in a subdomain only needs to be an order of magnitude less than the full-domain relative residual to achieve the convergence of the Gauss–Seidel or Jacobi iteration. Inaccurate approximate solutions from the Krylov solver are acceptable at the beginning of the iteration and the relative residual target of the Krylov solver is lowered as the full-domain relative solver is decreasing during the Gauss–Seidel or Jacobi iterative method. Additionally, the initial guess for the Krylov solver in the current outer iterative process is updated from the result of the previous outer iteration. Detailed implementation of this strategy is shown in Algorithm 1.

Although we did not use the contraction IE form in the derivation, the contraction IE pre-conditioning can be applied when solving the linear system of equations in each subdomain. This can result in further reduction of computation time pre-conditioning by improving the convergence rate of the Krylov solver in each subdomain (Endo *et al.* 2009; Zhdanov *et al.* 2006). Depending on the choice of Gauss–Seidel or Jacobi iteration, the contraction IE pre-conditioning can be applied when solving eq. (24) or (26).

Algorithm 1. IE method with domain decomposition pre-conditioning.

set : ϵ_t = threshold value, M = number of subdomains,
initialize : $\boldsymbol{E}^0 := \boldsymbol{E}^{(0)}$, $k := 1$
$\epsilon = \dfrac{\left\|\boldsymbol{E}^{(0)} - (\boldsymbol{I} - \boldsymbol{\mathcal{G}}_{\Delta\boldsymbol{\sigma}})\boldsymbol{E}^{k-1}\right\|}{\left\|\boldsymbol{E}^{(0)}\right\|}$
while $\epsilon > \epsilon_t$
 for $i = 1{:}\,M$
  if Gauss–Seidel pre-conditioning
   $\boldsymbol{b} = \boldsymbol{E}^{(i,0)} + \sum_{j=1}^{i-1}\boldsymbol{\mathcal{G}}^{(ij)}\Delta\boldsymbol{\sigma}^{(j)}\boldsymbol{E}^{(j),k+1} + \sum_{j=i+1}^{M}\boldsymbol{\mathcal{G}}^{(ij)}\Delta\boldsymbol{\sigma}^{(j)}\boldsymbol{E}^{(j),k}$
  else if Jacobi pre-conditioning
   $\boldsymbol{b} = \boldsymbol{E}^{(i,0)} + \sum_{j=1}^{M}\boldsymbol{\mathcal{G}}^{(ij)}\Delta\boldsymbol{\sigma}^{(j)}\boldsymbol{E}^{(j),k}$
  end if
  set : initial guess $= \boldsymbol{E}^{(i),k}$, threshold $= \epsilon/10$
  $\boldsymbol{E}^{(i),k+1} = \mathrm{GMRES}\left[\boldsymbol{A} = \left(\boldsymbol{I} - \boldsymbol{\mathcal{G}}^{(ii)}\Delta\boldsymbol{\sigma}^{(i)}\right), \boldsymbol{b}, \text{initial guess, threshold}\right]$
 end for
 $k = k + 1$
end while

3 NUMERICAL RESULTS AND DISCUSSION

In this section, we present three numerical cases to demonstrate the effectiveness of the domain decomposition pre-conditioning of the IE method. The first case is a model with two anomalous subdomains separated by an isotropic medium with conductivity equal to the background conductivity. In the second case, we present a model where the anomalous isotropic conductivity is surrounded by an anisotropic medium. Lastly, we simulate a logging scenario across a faulted sand formation surrounded by anisotropic shale layers. We use the IE formulation with contraction IE pre-conditioning as described in Section 2 in the GMRES solver for both full-domain IE and IE-DD method, which we refer to as full-domain CIE and CIE-DD, respectively. In all cases, we use the restarted GMRES method with 10 restart iterations. All numerical experiments presented in this paper are performed on a laptop with an AMD Ryzen 7 4800H processor and NVIDIA GeForce RTX 3060 Laptop GPU using MATLAB with GPU support enabled. We have compared our full-domain IE code with existing 1-D semi-analytical solution (Shahriari *et al.* 2018) and 3-D finite-volume method (Hou *et al.* 2006). This comparison is shown in Appendix B and our results show a good agreement with less than one per cent average absolute difference.

3.1 Isolated subdomains on isotropic medium example

We consider two isolated anomalous subdomains embedded in an isotropic medium background as shown in Fig. 2. The background conductivity σ_0 is equal to 0.1 S m^{-1} and the conductivity in the anomalous subdomain is equal to 0.01 S m^{-1}. A transmitter with a 24 kHz frequency is located at the origin ($x = 0$, $y = 0$, $z = 0$) and is oriented in the x-direction. The whole domain is discretized into 120 × 120 × 120 cubic grid blocks with a uniform grid size of 0.25 × 0.25 × 0.25 m^3. The two anomalous subdomains are set to have an equal size of 30 × 30 × 5 m^3 with the subdomain in the negative z-axis as the subdomain 1. The distance between the closest edges of the two subdomains is 10 m which is approximately equal to the skin depth of the background medium given the transmitter frequency.

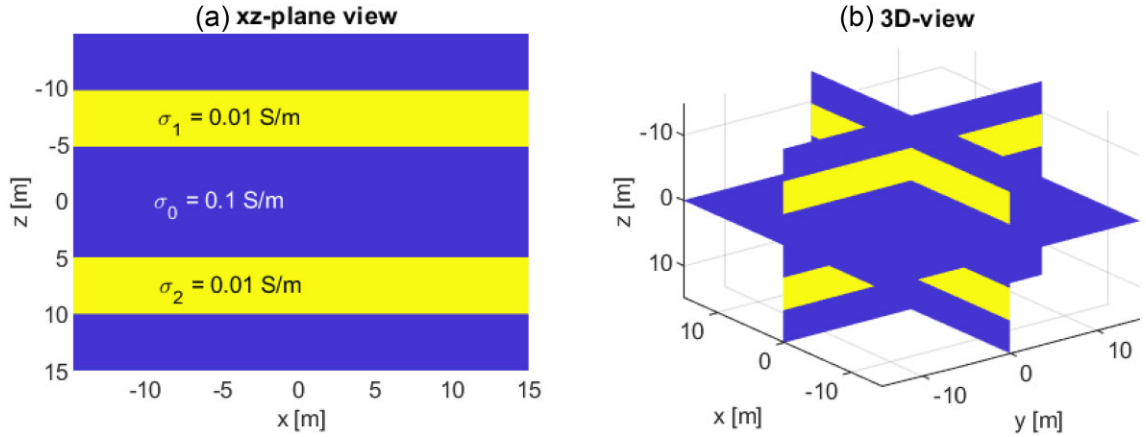

Figure 2. (a) *xz*-plane view of the model at $y = 0$ m. (b) *xy*- and *xz*-slice of the model in 3-D view.

We set the full-domain relative residual to $\epsilon_f = 10^{-6}$ for both the full-domain CIE and CIE-DD iteration stopping criterion. Because the medium without contrast does not contribute to the scattering field, we refer to the full-domain relative residuals as the relative residual evaluated within the anomalous subdomains in both cases. Additionally, the subdomains without the conductivity anomalies are excluded from the discretization in the CIE-DD iterations. This results in one-third of the total number of grid blocks of the full-domain IE being discretized in the CIE-DD iterations.

We present four different schemes of CIE-DD to calculate the electric field of the model, which are CIE-DD-GS-F, CIE-DD-GS-A, CIE-DD-J-F and CIE-DD-J-A. The letters GS and J refer to the CIE-DD with Gauss–Seidel and Jacobi iteration, respectively. The letter F denotes the CIE-DD with a fixed GMRES solver relative residual stopping criterion equal to 10^{-6} in every outer iteration. Whereas the letter A denotes the implementation of adaptive GMRES solver relative residual stopping criterion. In the adaptive relative residual scheme, the relative residual stopping criterion is set to be one order of magnitude lower than the relative residual calculated on the domain of interest or the full-domain relative residual of the current outer iteration divided by ten.

The full-domain relative residuals presented in Fig. 3 shows the convergence behaviour of all the CIE-DD schemes. It can be seen that all the schemes are converged to the desired tolerance level. In general, the relative residuals are decreasing at almost a constant rate in all schemes, which are indicated by almost linear slopes in the plot with a logarithmic scale. These rates are higher in the schemes with Gauss–Seidel iterations compared to the ones with Jacobi iterations. Comparing different GMRES solver tolerance schemes, these convergence rates are higher in the schemes with fixed GMRES solver tolerance. However, it can be observed that there are decreases in the convergence rate in the last iteration which is not the case with the adaptive tolerance schemes.

The full-domain relative residual behaviours indicate that the convergence rates of the CIE-DD schemes are related to the ratio between the full-domain relative residual and the GMRES solver tolerance in the current outer iteration. In the schemes with fixed GMRES solver tolerance of 10^{-6}, the ratios decrease as the full-domain relative residual approaches 10^{-6}. This may explain the significant changes of the line slopes at the last iteration of the schemes with fixed tolerance in Fig. 3. Whereas in the adaptive tolerance scheme, this ratio is approximately constant in each outer iteration which reflects the almost constant line slopes in the full-domain relative residual plot.

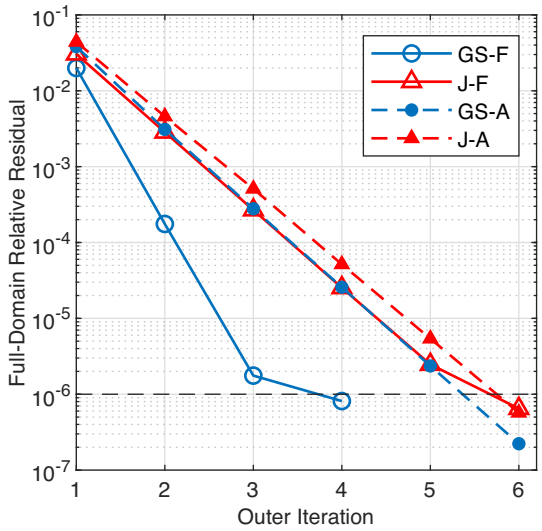

Figure 3. Full-domain relative residual during the Gauss–Seidel and Jacobi iteration of the CIE-DD schemes. The solid and dashed lines indicate the schemes with fixed and adaptive GMRES tolerance, respectively.

Fig. 4 displays the total number of GMRES iterations taken to reach the target residual within each of the outer iteration corresponding to the Gauss–Seidel and Jacobi iteration. The schemes with fixed GMRES solver tolerance show a decreasing trend of the total number of GMRES iterations with the number of outer iterations. This indicates that the changes in the electric fields due to the interaction terms become smaller as the initial guess for the GMRES solver is updated in each of the outer iterations. On the other hand, these numbers are generally increasing in the schemes with adaptive GMRES solver tolerance which is related to the increasing difficulty of reaching lower tolerance in each outer iteration. It can be observed that the total GMRES iterations in subdomains 1 and 2 are equal in the Jacobi schemes due to the symmetry of the subdomains.

Table 1 summarizes the computational cost comparison between the full-domain CIE and CIE-DD with different schemes. All the CIE-DD schemes converge below the desired tolerance within six outer iterations. It can be seen that the total GMRES iterations in

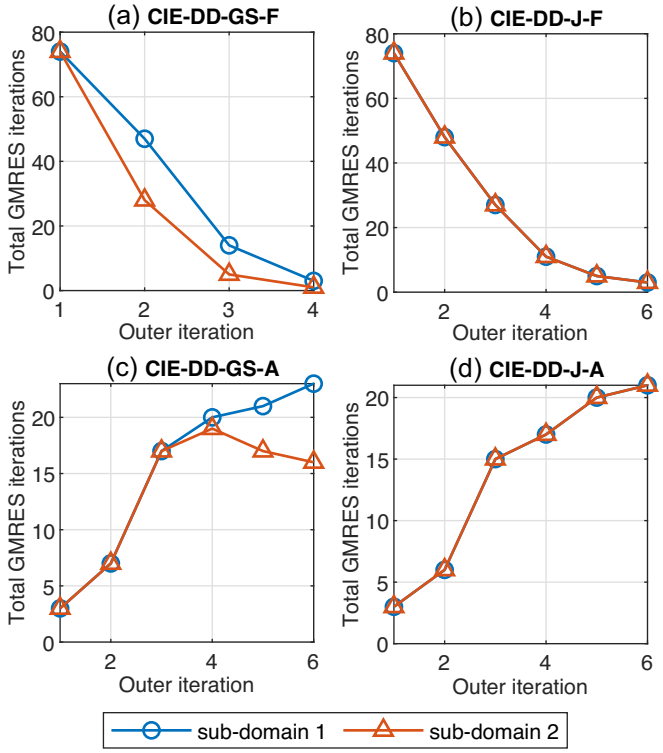

Figure 4. Total number of GMRES solver iterations within each outer iteration corresponding to the Gauss–Seidel (left-hand column) or Jacobi (right-hand column) iterations. The plots in the top and bottom rows contain the schemes with fixed and adaptive GMRES solver tolerance, respectively.

Table 1. Computational cost of IE with different schemes on the isolated domain case.

Schemes	Target ϵ_s	Total GMRES iterations	Total outer iterations	Time (s)
Full-domain CIE	10^{-6}	75	–	12.42
CIE-DD-GS-F	10^{-6}	246	4	8.73
CIE-DD-J-F	10^{-6}	336	6	11.86
CIE-DD-GS-A	$\epsilon_f/10$	170	6	6.29
CIE-DD-J-A	$\epsilon_f/10$	164	6	6.19

Note. ϵ_s and ϵ_f are the relative residual of the sub- and full domains, respectively.

the CIE-DD schemes are more than the full-domain CIE, but the computation time is faster than the full-domain CIE. This is because the GMRES iterations in CIE-DD work on a smaller domain with the number of blocks equal to one-sixth of the full-domain grid blocks in each domain.

Based on the computation time, the schemes with domain decomposition method with adaptive GMRES solver tolerance are faster compared to their fixed tolerance counterparts. The CIE-DD-GS-A schemes show faster computation time compared to the CIE-DD-GS-F schemes because there are fewer GMRES iterations. Therefore, specifying the adaptive relative residual for the Krylov solver in the CIE-DD improves the computation time of the original CIE-DD formulation with the cost of going through more outer iterations. Compared to the full-domain CIE, the computation time using CIE-DD-GS-A and CIE-DD-J-A schemes are faster by approximately factors of 1.97 and 2, respectively. The CIE-DD-J-A is slightly faster compared to the CIE-DD-GS-A in this example because it takes slightly fewer number GMRES iterations.

Fig. 5 shows the total magnetic field comparison between the results calculated using full-domain CIE, CIE-DD-GS-A and CIE-DD-J-A. Qualitatively, there are no differences observed because both methods show similar numerical results within less than 0.01 per cent average normalized magnitude difference. Therefore, the CIE-DD method will give the same result within the same relative residual level as the full-domain CIE.

3.2 Simple faulted anisotropic medium example

Fig. 6 shows an *xz*-plane view of a faulted resistive isotropic medium with a conductivity of 0.005 S m^{-1} surrounded by an anisotropic medium with vertical transverse isotropy. The conductivity tensor of the anisotropic medium consists of the conductivity in the horizontal and vertical directions with the value of $\sigma_h = 0.2$ S m^{-1} and $\sigma_v = 0.1$ S m^{-1}, respectively. The conductivity of the media does not vary in the *y*-direction. For the background medium, we choose a homogenous isotropic medium with a conductivity of $\sigma_0 = 0.1$ S m^{-1}. A transmitter with a 24 kHz frequency is located at the origin and is oriented in the *x*-direction. The whole domain is discretized into 120 × 120 × 120 grid blocks with a grid size of 0.25 × 0.25 × 0.25 m^3. Because the whole domain contains conductivity anomalies with respect to the background conductivity, there is no reduction in discretization in the CIE-DD method. We set the full-domain relative residual to $\epsilon_f = 10^{-6}$ as the stopping criterion for the full-domain CIE and CIE-DD.

The full domain is decomposed into three rectangular subdomains of equal size as illustrated in Fig. 6. Each subdomain is discretized into 120 × 120 × 40 grid blocks with a grid size of 0.25 × 0.25 × 0.25 m^3. With this decomposition, the faulted resistive layer is located only in subdomain 1, while the other two

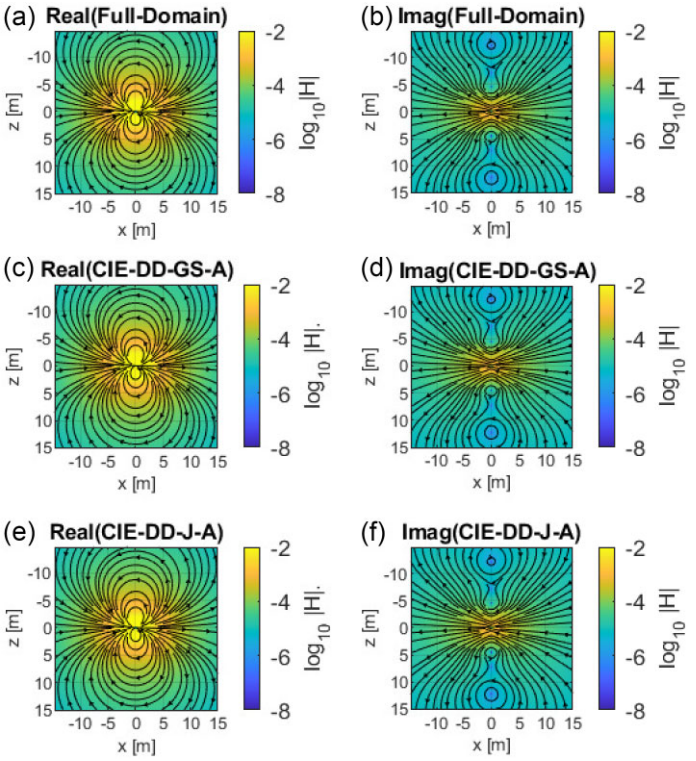

Figure 5. *xz*-plane slice of total magnetic fields at $y = 0$ m. A transmitter oriented in the x-direction is located at $x = 0$ m, $y = 0$ m and $z = 0$ m. From top to bottom row: full-domain CIE, CIE-DD-GS-A and CIE-DD-J-A. The real and imaginary parts of the magnetic fields are on the left- and right-hand columns, respectively.

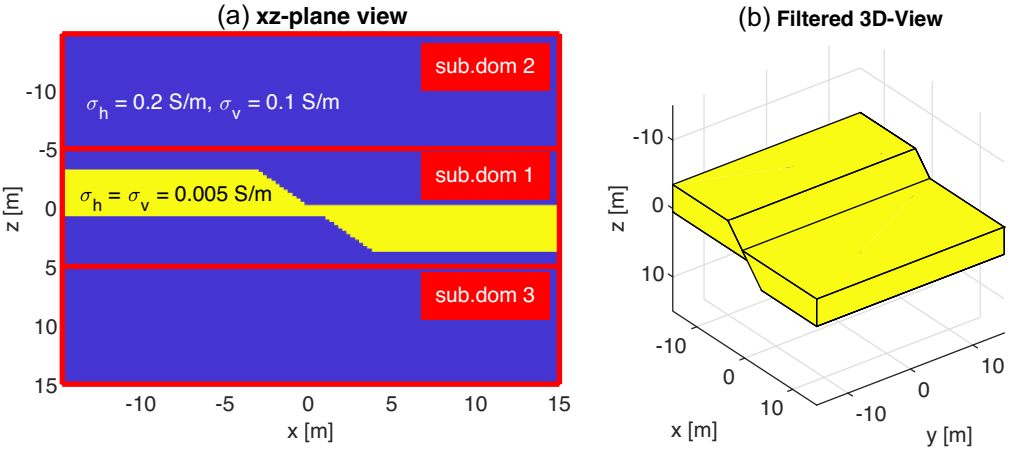

Figure 6. (a) *xz*-plane view of a faulted resistive layer surrounded by an anisotropic medium at $y = 0$ m and the domain decomposition setting. (b) 3-D view with the anisotropic layers removed. A transmitter oriented to the x-direction is located at $x = 0$ m, $y = 0$ m and $z = 0$ m.

subdomains contain only the anisotropic medium. In this example, we present the results of using the CIE-DD-GS-A and CIE-DD-J-A schemes. In both schemes, we set GMRES solver stopping criterion equals the maximum between $\epsilon_f/10$ and 10^{-6}. With this slight modification, we minimize the number of GMRES iterations taken when the full-domain residual in the outer iteration is close to its stopping criterion.

Full-domain relative residuals presented in Fig. 7 show the convergence of both CIE-DD-GS-A and CIE-DD-Jacobi schemes. The full-domain relative residuals with both schemes are always decreasing with outer iteration to the desired tolerance. In general, the convergence rate of the CIE-DD-GS-A is faster than the CIE-DD-J-A. The CIE-DD-GS-A converges within seven outer iterations, while the CIE-DD-J-A converges within 10 outer iterations.

The computational cost comparison between the full-domain CIE and CIE-DD schemes is shown in Table 2. In this case, the total number of GMRES iterations for the CIE-DD is similar value to the total number of iterations for the full-domain CIE. Because the computational cost of a GMRES iteration in the CIE-DD method is cheaper, this results in the computation time reduction for both the CIE-DD-GS-A and CIE-DD-Jac-A schemes of approximately a factor of 2.84 compared to the full-domain CIE. We have tested

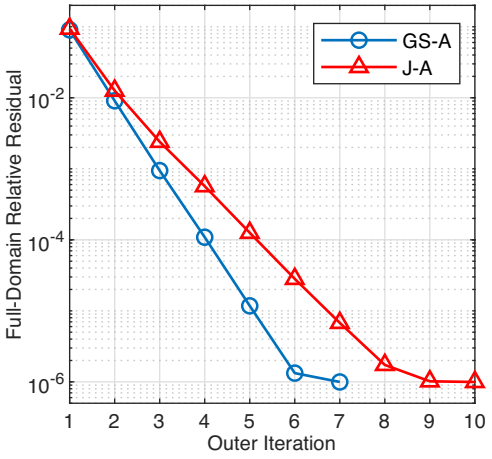

Figure 7. The convergence rate comparison between the CIE-DD-GS-A and CIE-DD-J-A schemes for the anisotropic medium example.

Table 2. Comparison of computational cost and resulting relative residual of different IE schemes on the anisotropic medium example.

Schemes	Total GMRES iterations	Total outer iterations	Time (s)	ϵ_f
Full-domain CIE	18600	–	3053.87	9.99×10^{-7}
CIE-DD-GS-A	18163	7	1075.50	9.97×10^{-7}
CIE-DD-J-A	18329	10	1083.09	9.96×10^{-7}

the CIE-DD-GS-A with different subdomain order and the effect of changing the order is not significant to be included in this paper.

Fig. 8 displays the distribution of total number of GMRES iterations in each subdomain for every outer iteration using CIE-DD-GS-A and CIE-DD-J-A schemes. In both cases, subdomain 1, which contains the faulted resistive layer, takes the largest number of GMRES iterations. The total number of GMRES iterations in subdomain 1 increases up to 4770 while it is only below 10 in the other two subdomains. This indicates different condition numbers in each subdomain which can be related to the conductivity contrast in the domain (Singer *et al.* 2003; Zaslavsky *et al.* 2011; Yavich & Zhdanov 2016). Yavich & Zhdanov (2016) established that the condition number is bounded by the maximum conductivity contrast between the actual and background conductivity. The maximum ratio of actual to background conductivity is a factor of 10 in the subdomain 1, while it is a factor of two in the other subdomains. Based on these factors, subdomain 1 has the highest contrast compared to the other subdomains.

This example highlights the usage of the domain decomposition method for isolating the domain with the highest condition number and reducing the computation time. By isolating the subdomain with the highest contrast, we can exclude the calculation in the subdomain with less contrast and focus the computational resource on iterating in this domain.

3.3 Logging simulation across a complex formation

We simulated induction logs across the faulted anisotropic formation with an 85° drilling angle as illustrated in Fig. 9(a). This formation consists of anisotropic shale layers surrounding isotropic sand layers. The shale layers are marked in blue and the sand layers in yellow in Fig. 9. The model has 2.5-D main structural features with the addition of a simple 3-D Gaussian perturbation only in the sand layers to imitate a fluid distribution in a reservoir. This perturbation is defined by

$$\boldsymbol{\sigma}_{\text{sand}} = \boldsymbol{\sigma}^{u}_{\text{sand}} + \alpha \boldsymbol{\sigma}^{u}_{\text{sand}} \exp\left(-\frac{|\boldsymbol{r}_{\text{sand}} - \boldsymbol{r}_c|}{\gamma}\right), \tag{27}$$

where the subscripts sand denote the values located in the sand layers and the superscripts u indicate the defined unperturbed value; $\boldsymbol{r}_c$ is the location of the maximum perturbation; α and γ are the factors that control the magnitude and range of the perturbation, respectively. In this example, we set the peak perturbation location $\boldsymbol{r}_c$ at $x = 500$ m, $y = 0$ m and $z = 40$ m; and define $\alpha = 4$ and $\gamma = 50$ m.

We use a moving 3-D forward modelling window to simulate a moving transmitter scenario. The z-direction in the forward modelling window is directed to the drilling direction so it is consistent with the component direction of the induction tools (Pardo & Torres-Verdín 2015). Hence, the coordinate system in the window is rotated from the Cartesian coordinate system according to the drilling direction as illustrated in Fig. 9(a). Consequently, the conductivity tensor elements are transformed following the domain rotation (Gao 2006), see Appendix C for further details. In each of the forward modelling windows, we set a constant background conductivity $\sigma_0 = 0.1$ S m^{-1}.

Following the typical tool configurations described in Antonsen *et al.* (2022), we set a z-oriented transmitter with a frequency of 24 kHz and three receivers with spacings of 7, 15 and 30 m as illustrated in Fig. 10 for the logging simulations. A forward modelling window with a size of $32 \times 32 \times 32$ m^3 may not be enough to capture the full sensitivity of all the receivers, especially the one with the largest spacing. Hence, we tested two different windows with different sizes of $32 \times 32 \times 64$ and $64 \times 64 \times 64$ m^3 to see different sensitivities of the receivers with the forward modelling domain size. We refer to the smaller window as window 1 and the larger one as window 2. In both windows, we keep a grid size of $0.25 \times 0.25 \times 0.25$ m^3 resulting in a total of $128 \times 128 \times 256$ and $256 \times 256 \times 256$ grid blocks for windows 1 and 2, respectively.

The memory requirement of solving a linear system of equations using iterative methods and FFT convolution roughly scales linearly with the number of grid blocks N. The memory requirements for storing the electric fields and conductivity model remain the same with and without domain decomposition. However, because the GMRES solver and FFT convolution operations are done on each subdomain separately using the domain decomposition method, the memory requirement for GMRES solver and FFT convolution operations can be reduced from O(N) to O(N/M), with M the number of subdomains. This allows us to fully take advantage of the GPU acceleration with limited GPU memory and solve a large linear system of IE without having to store everything in the memory at the same time.

The logging position starts at $x = 0$ m, $y = 0$ m and $z = 0$ m and ends at $x = 900$ m, $y = 0$ m and $z = 78.74$ m. In each logging position, we use the CIE-DD-GS-A scheme and we set the order of the subdomain according to the distance of the subdomain closest edges to the source point as shown in Fig. 11. We set $\epsilon_f = 10^{-3}$ as the outer iteration stopping criteria as it is good enough to see the main pattern of $|H_{zz}|$ component at the receiver positions along the drilling trajectory.

Fig. 12 shows $|H_{zz}|$ component measured by the receivers at each transmitter position using different windows. Qualitatively, the differences in the results between the two window settings are increasing with the receiver spacings. This result shows different

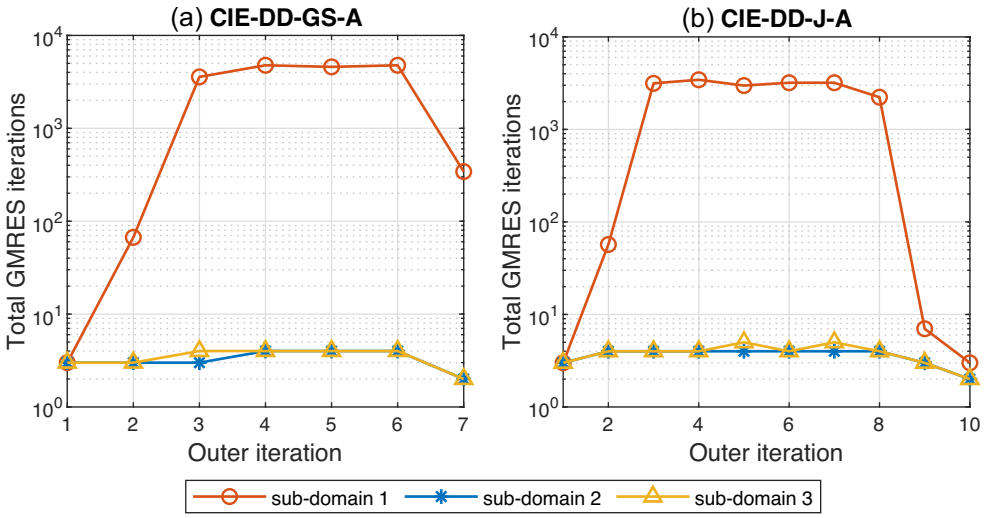

Figure 8. Total GMRES iterations within each (a) CIE-DD-GS-A and (b) CIE-DD-J-A schemes for the anisotropic medium example.

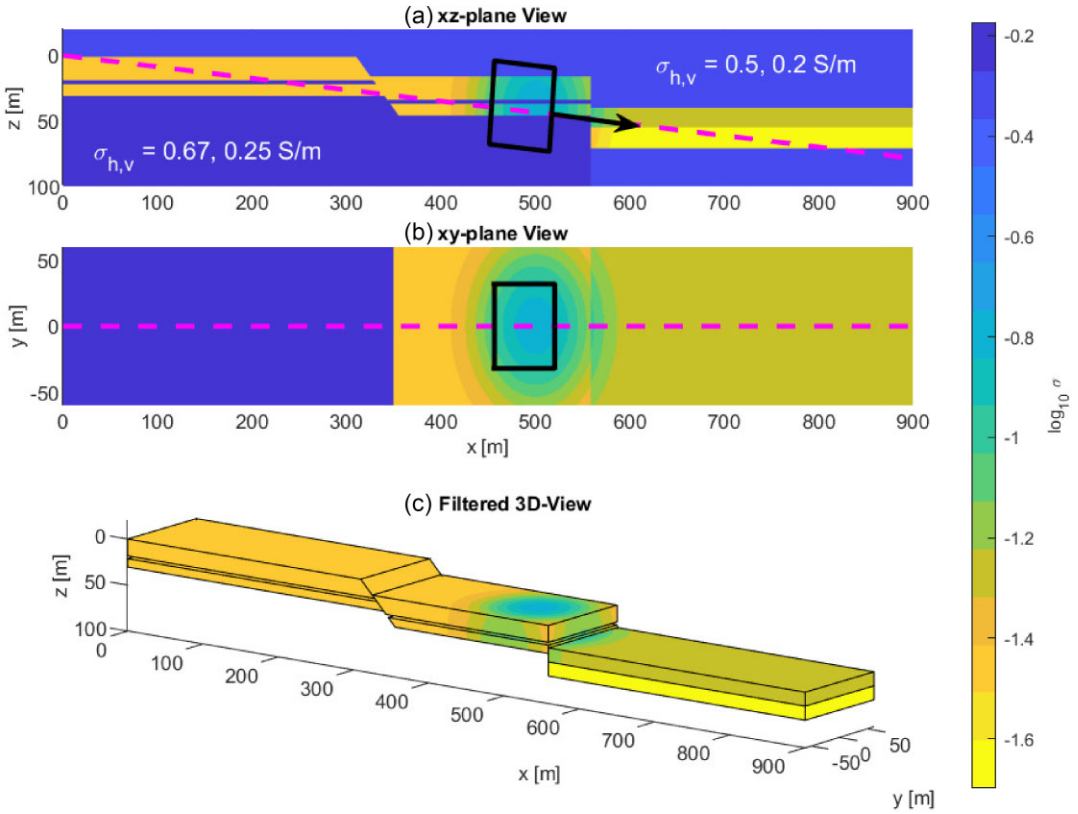

Figure 9. (a) *xz*-plane view at $y = 0$ m. (b) *xy*-plane view at $z = 40$ m. (c) 3-D view of the model with the shale layers removed. The magenta dashed lines indicate the drilling trajectory. The black box is a forward modelling window example with a size of $64 \times 64 \times 64$ m^3 at one logging position.

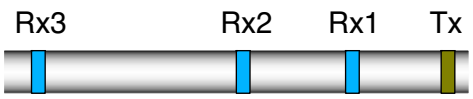

Figure 10. Illustration of an induction tool with a single transmitter and three receivers. Tx and Rx stand for transmitter and receiver, respectively.

sensitivities of the transmitter–receiver spacing and we can observe that the sensitivity range is proportional to the receiver spacing.

The computation time required to calculate the magnetic field for one logging position using the windows 1 and 2 settings takes an average of approximately 54.28 and 633.77 s, respectively. Updating the interaction terms is the most expensive part of the computation time, taking up around 80 per cent of the time at every iteration. One of the main reasons is that the FFT of dyadic Green's tensors for the interaction terms is not pre-calculated before the Gauss–Seidel iterations due to not enough memory space available to store these tensors. This adds extra FFT function calls which can be avoided when the dyadic Green's operators can be put into memory.

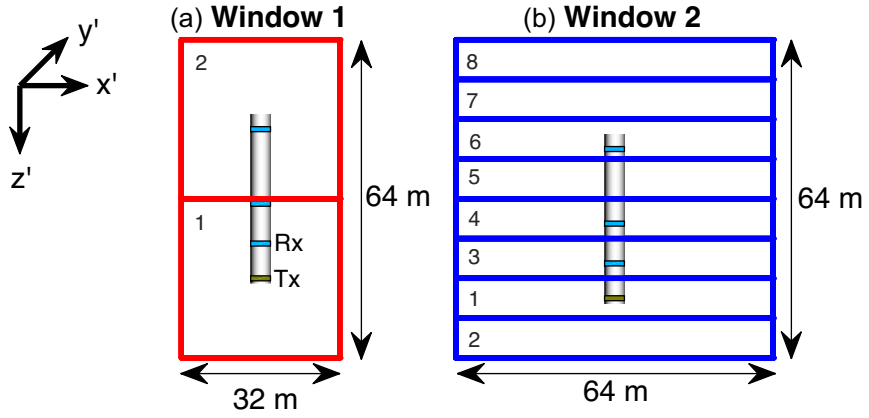

Figure 11. Domain decomposition illustration of (a) window 1 and (b) window 2. z'-axis is the drilling direction. The range in the y'-direction is equal to the range in the x'-direction. The numbers inside the windows denote the subdomain order.

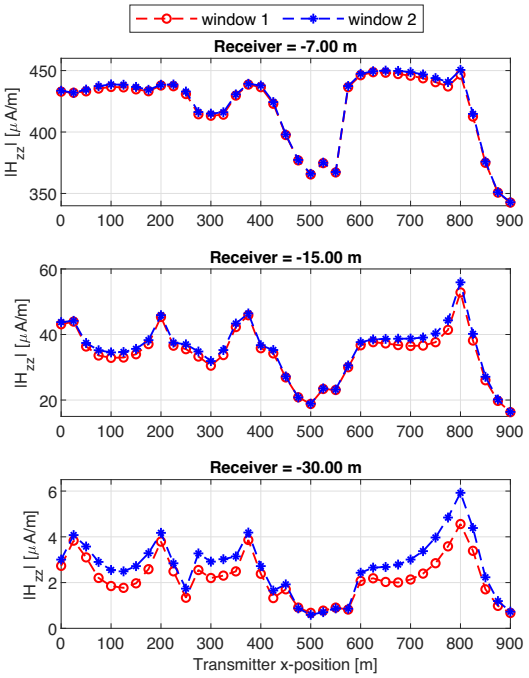

Figure 12. Measured magnitude of the z-component $|H_{zz}|$ at different receiver positions across the formation.

In every position, it took three to four Gauss–Seidel iterations with 49–86 total GMRES iterations to reach the desired tolerance using the window 1 setting. Whereas using the window 2 setting, it took four to seven Gauss–Seidel iterations with 293–424 total GMRES iterations in each logging position.

4 CONCLUSION

The linear system of equations arising in the IE method for 3-D EM method modelling can be naturally decomposed into a set of linear systems of equations that correspond to the IE in different parts of the modelling domain. The IE-DD formulation reduces the memory requirement to compute a large-scale problem as it provides the connection between each subdomain while still maintaining the viability of using FFTs to calculate the convolution integral operation. By expressing these linear systems of equations in a block matrix representation where each block represents the interactions between the domains, we have made a link between the derivation in Zhdanov *et al.* (2006) and Endo *et al.* (2009) with a pre-conditioned fixed-point iteration using domain decomposition method. Depending on the choice of the pre-conditioner, the fixed-point iteration corresponds to the block Gauss–Seidel and Jacobi iterative method. In every Gauss–Seidel or Jacobi iteration, the inverse of the block intradomain interaction term is calculated using the Krylov subspace method instead of a direct solver. In addition to the domain decomposition method, we use the implementation of contraction integral pre-conditioner when solving the linear system in each subdomain.

Our numerical results show that a reduction in computation time can be achieved although the total number of GMRES solver iterations in IE-DD schemes is more than in the full-domain IE. This speed-up is due to the GMRES solver in the decomposed domains being cheaper to compute and it is shown that it only takes less than 10 IE-DD outer iterations to reach the desired tolerance. Additionally, specifying adaptive relative residual stopping improves the computation time of the IE-DD by reducing the total number of GMRES iterations required for reaching the desired error tolerance. The implementation of domain decomposition shows the advantage of reduction in discretization and isolating subdomain with high contrast. Our numerical experiments show computation time reductions by factors of 1.97–2.84 compared to the full-domain pre-conditioned IE. In addition, the domain decomposition method can be used to reduce the memory requirements of the operations involved in solving a large system of IE. The IE-DD with Gauss–Seidel pre-conditioning generally has a better convergence rate compared to the Jacobi pre-conditioning. However, the form of the Jacobi iterative method is more suitable for parallel computation as the operation in each subdomain can be computed independently, which is a subject for future implementation.

In this study, we have only implemented IE-DD with a simple iterative update corresponding to the Gauss–Seidel and Jacobi iterative methods. The Gauss–Seidel and Jacobi iterative methods are in general not very competitive in terms of convergence compared to the Krylov subspace method (Barrett *et al.* 1994). Therefore, further potential improvement of the IE-DD presented in this study is obtained by implementing the Krylov subspace as the outer iteration update instead of the Gauss–Seidel and Jacobi iteration update. Another interesting application of the domain decomposition in the IE method would be to incorporate a direct method that can be computed in parallel into the domain decomposition pre-conditioner, for

example using the *T*-matrix method (Jakobsen & Tveit 2018; Sommer & Jakobsen 2018). Since the domain decomposition method can be used for solving any linear system of equations in general, it can be applied to other numerical or geophysical methods that involve solving a linear system of equations.

ACKNOWLEDGMENTS

This work is part of the Center for Research-based Innovation DigiWells: Digital Well Center for Value Creation, Competitiveness and Minimum Environmental Footprint (NFR SFI project no. 309589, https://DigiWells.no). The centre is a cooperation of NORCE Norwegian Research Centre AS, the University of Stavanger, the Norwegian University of Science and Technology (NTNU) and the University of Bergen. It is funded by Aker BP, ConocoPhillips, Equinor, Lundin Energy, TotalEnergies, Vår Energi, Wintershall Dea and the Research Council of Norway. The authors would like to acknowledge the involvement in 3D geological interpretation for geosteering of wells project (project no. 336385).

DATA AVAILABILITY

Currently, the data and codes relating to this work are not freely available. We are considering publishing the codes with an open-source license in the future.

REFERENCES

Antonsen, F., Danielsen, B.E., Jensen, K.R., Prymak-Moyle, M., Lotsberg, J.K., Teixeira De Oliveira, M.E. & Constable, M.V., 2022. What next after a decade with significant advances in the application of ultradeep azimuthal resistivity measurements?, *Petrophysics,* **63**(06), 762–780.

Avdeev, D.B., 2005. Three-dimensional electromagnetic modelling and inversion from theory to application, *Surv. Geophys.,* **26**(6), 767–799.

Bakr, S.A., Pardo, D. & Torres-Verdín, C., 2017. Fast inversion of logging-while-drilling resistivity measurements acquired in multiple wells, *Geophysics,* **82**(3), E111–E120.

Barrett, R. *et al.*, 1994. *Templates for the Solution of Linear Systems: Building Blocks for Iterative Methods,* SIAM.

Chen, C., Kruglyakov, M. & Kuvshinov, A., 2021. Advanced three-dimensional electromagnetic modelling using a nested integral equation approach, *Geophys. J. Int.,* **226**(1), 114–130.

Dyatlov, G., Onegova, E. & Dashevsky, Y., 2015. Efficient 2.5D electromagnetic modeling using boundary integral equations, *Geophysics,* **80**(3), E163–E173.

Endo, M., Čuma, M. & Zhdanov, M.S., 2009. Large-scale electromagnetic modeling for multiple inhomogeneous domains, *Commun. Comput. Phys.,* **6**(2), 269–289.

Fang, S., Gao, G. & Verdin, C.T., 2006. Efficient 3D electromagnetic modelling in the presence of anisotropic conductive media, using integral equations, *Explor. Geophys.,* **37**(3), 239–244.

Gao, G., 2006. *Simulation of Borehole Electromagnetic Measurements in Dipping and Anisotropic Rock Formations and Inversion of Array Induction Data,* The University of Texas at Austin.

Gao, G., Torres-Verdin, C. & Habashy, T., 2005. Analytical techniques to evaluate the integrals of 3D and 2D spatial dyadic Green's functions, *Prog. Electromag. Res.,* **52,** 47–80, Citeseer.

Gibson, W.C., 2021. *The Method of Moments in Electromagnetics,* CRC Press.

Hou, J., Mallan, R.K. & Torres-Verdín, C., 2006. Finite-difference simulation of borehole em measurements in 3D anisotropic media using coupled scalar-vector potentials, *Geophysics,* **71**(5), G225–G233.

Hursan, G. & Zhdanov, M.S., 2002. Contraction integral equation method in three-dimensional electromagnetic modeling, *Radio Sci.,* **37**(6), 1–13.

Jahani, N., Torres-Verdín, C., Hou, J. & Tveranger, J., 2023. Limits of 3D detectability and resolution of LWD deep-sensing borehole electromagnetic measurements acquired in the Norwegian Continental Shelf, in *SPWLA Annual Logging Symposium,* p. D041S008R005, SPWLA.

Jakobsen, M. & Tveit, S., 2018. Distorted born iterative t-matrix method for inversion of CSEM data in anisotropic media, *Geophys. J. Int.,* **214**(3), 1524–1537.

Kamm, J. & Pedersen, L.B., 2014. Inversion of airborne tensor vlf data using integral equations, *Geophys. J. Int.,* **198**(2), 775–794.

Newman, G.A. & Alumbaugh, D.L., 2002. Three-dimensional induction logging problems, part 2: a finite-difference solution, *Geophysics,* **67**(2), 484–491.

Nie, X.C., Yuan, N. & Liu, R., 2013. A fast integral equation solver for 3d induction well logging in formations with large conductivity contrasts, *Geophys. Prospect.,* **61**(3), 645–657.

Noh, K., Torres-Verdín, C. & Pardo, D., 2022. Real-time 2.5 D inversion of LWD resistivity measurements using deep learning for geosteering applications across faulted formations, *Petrophysics,* **63**(04), 506–518.

Pardo, D. & Torres-Verdín, C., 2015. Fast 1D inversion of logging-while-drilling resistivity measurements for improved estimation of formation resistivity in high-angle and horizontal wells, *Geophysics,* **80**(2), E111–E124.

Puzyrev, V., 2019. Deep learning electromagnetic inversion with convolutional neural networks, *Geophys. J. Int.,* **218**(2), 817–832.

Puzyrev, V., Koldan, J., de la Puente, J., Houzeaux, G., Vázquez, M. & Cela, J.M., 2013. A parallel finite-element method for three-dimensional controlled-source electromagnetic forward modelling, *Geophys. J. Int.,* **193**(2), 678–693.

Puzyrev, V., Pardo, D., Calo, V. & Torres-Verdín, C., 2019. Recent advances on the inversion of deep directional borehole resistivity measurements, *ASEG Extended Abstr.,* **2019**(1), 1–3.

Ren, Z., Kalscheuer, T., Greenhalgh, S. & Maurer, H., 2014. A hybrid boundary element-finite element approach to modeling plane wave 3*D* electromagnetic induction responses in the Earth, *J. Comput. Phys.,* **258,** 705–717.

Saad, Y., 2003. *Iterative Methods for Sparse Linear Systems,* SIAM.

Saad, Y. & Schultz, M.H., 1986. GMRES: A generalized minimal residual algorithm for solving nonsymmetric linear systems, *SIAM J. Sci. Stat. Comput.,* **7**(3), 856–869.

Saputera, D., Jakobsen, M., Jahani, N., Alyaev, S., Eikrem, K. & van Dongen, K.W.A., 2022. GPU-accelerated integral equation method for 3D modelling of induction logs, in *Presented at Geosteering and Formation Evaluation Workshop by NFES and NORCE*. The Norwegian Formation Evaluation Society (NFES).

Shahriari, M., Rojas, S., Pardo, D., Rodríguez-Rozas, A., Bakr, S.A., Calo, V.M. & Muga, I., 2018. A numerical 1.5 D method for the rapid simulation of geophysical resistivity measurements, *Geosciences,* **8**(6), 225.

Singer, B.S., Mezzatesta, A. & Wang, T., 2003. Integral equation approach based on contraction operators and krylov subspace optimisation, *ASEG Extended Abst.,* **2003**(1), 1–14.

Sinha, S. *et al.*, 2022. Past, present, and future applications of ultradeep directional resistivity measurements: a case history from the norwegian continental shelf, *Petrophysics – SPWLA J. Form. Eval. Reserv. Descrip.,* **63**(6), 604–633.

Sommer, M. & Jakobsen, M., 2018. Towards a fast integral equation method for inversion of electromagnetic data, in *Second EAGE/SPE Geosteering and Well Placement Workshop,* vol. **2018,** pp. 1–5, EAGE Publications BV.

Van Dongen, K.W.A., Brennan, C. & Wright, W.M., 2007. Reduced forward operator for electromagnetic wave scattering problems, *IET Sci. Measure. Technol.,* **1**(1), 57–62.

Venkateshan, S.P. & Swaminathan, P., 2014. Chapter 2 - solution of linear equations, in *Computational Methods in Engineering,* pp. 19–103, eds Venkateshan, S.P. & Swaminathan, P., Academic Press, Boston.

Wang, B., Jakobsen, M., Wu, R.-S., Lu, W. & Chen, X., 2017. Accurate and efficient velocity estimation using transmission matrix formalism based on the domain decomposition method, *Inverse Probl.,* **33**(3), 035002, doi: 10.1088/1361-6420/aa5998.

Wang, B., Liu, J., Hu, X., Liu, J., Guo, Z. & Xiao, J., 2021. Geophysical electromagnetic modeling and evaluation: a review, *J. appl. Geophys.*, **194,** 104438, doi: 10.1016/j.jappgeo.2021.104438.

Wannamaker, P.E. & Zhdanov, M.S., 2002. *Three-Dimensional Electromagnetics,* Elsevier.

Wilson, G., Marchant, D., Haber, E., Clegg, N., Zurcher, D., Rawsthorne, L. & Kunnas, J., 2019. Real-time 3D inversion of ultra-deep resistivity logging-while-drilling data, in *SPE Annual Technical Conference and Exhibition,* OnePetro. D012S062R001 SPE.

Yavich, N. & Zhdanov, M.S., 2016. Contraction pre-conditioner in finite-difference electromagnetic modelling, *Geophys. J. Int.,* **206**(3), 1718–1729.

Yoon, D., Zhdanov, M.S., Mattsson, J., Cai, H. & Gribenko, A., 2016. A hybrid finite-difference and integral-equation method for modeling and inversion of marine controlled-source electromagnetic data, *Geophysics,* **81**(5), E323–E336.

Zaslavsky, M., Druskin, V., Davydycheva, S., Knizhnerman, L., Abubakar, A. & Habashy, T., 2011. Hybrid finite-difference integral equation solver for 3D frequency domain anisotropic electromagnetic problems, *Geophysics,* **76**(2), F123–F137.

Zhdanov, M.S., 2009. *Geophysical Electromagnetic Theory and Methods,* Elsevier.

Zhdanov, M.S., Lee, S.K. & Yoshioka, K., 2006. Integral equation method for 3D modeling of electromagnetic fields in complex structures with inhomogeneous background conductivity, *Geophysics,* **71**(6), G333–G345.

APPENDIX A: FORWARD SUBSTITUTION IN GAUSS–SEIDEL ITERATIVE METHOD

The inverse of a lower triangular matrix can be obtained through forward substitution (Venkateshan & Swaminathan, 2014). For simplicity, we demonstrate the forward-substitution process in the case of domain decomposition with three subdomains. We can write the block-matrix representation and its splitting for three subdomains:

$$A = \begin{bmatrix} \boldsymbol{A}_{11} & \boldsymbol{A}_{12} & \boldsymbol{A}_{13} \\ \boldsymbol{A}_{21} & \boldsymbol{A}_{22} & \boldsymbol{A}_{23} \\ \boldsymbol{A}_{31} & \boldsymbol{A}_{32} & \boldsymbol{A}_{33} \end{bmatrix} = (\boldsymbol{D} + \boldsymbol{L} + \boldsymbol{U}), \tag{A1}$$

with the matrices $\boldsymbol{D}$, $\boldsymbol{L}$ and $\boldsymbol{U}$ are the block diagonal, strictly lower triangular and strictly upper triangular of $\boldsymbol{A}$, respectively. These terms are defined as

$$\boldsymbol{D} = \begin{bmatrix} \boldsymbol{A}_{11} & \boldsymbol{0} & \boldsymbol{0} \\ \boldsymbol{0} & \boldsymbol{A}_{22} & \boldsymbol{0} \\ \boldsymbol{0} & \boldsymbol{0} & \boldsymbol{A}_{33} \end{bmatrix},$$

$$\boldsymbol{L} = \begin{bmatrix} \boldsymbol{0} & \boldsymbol{0} & \boldsymbol{0} \\ \boldsymbol{A}_{21} & \boldsymbol{0} & \boldsymbol{0} \\ \boldsymbol{A}_{31} & \boldsymbol{A}_{32} & \boldsymbol{0} \end{bmatrix}, \tag{A2}$$

and

$$\boldsymbol{U} = \begin{bmatrix} \boldsymbol{0} & \boldsymbol{A}_{12} & \boldsymbol{A}_{13} \\ \boldsymbol{0} & \boldsymbol{0} & \boldsymbol{A}_{23} \\ \boldsymbol{0} & \boldsymbol{0} & \boldsymbol{0} \end{bmatrix}.$$

Here, each of the blocks denotes the interdomain or intradomain operators described in Section 2 as

$$\boldsymbol{A}_{ii} = \left(\boldsymbol{I} - \boldsymbol{\mathcal{G}}^{(ii)} \Delta \boldsymbol{\sigma}^{(i)}\right), \tag{A3}$$

$$\boldsymbol{A}_{ij} = -\boldsymbol{\mathcal{G}}^{(ij)} \Delta \boldsymbol{\sigma}^{(j)}, \quad i \neq j. \tag{A4}$$

The fixed-point equations using matrix **A** that corresponds to the Gauss–Seidel iterative method

$$\widetilde{\boldsymbol{E}}^{k+1} = (\boldsymbol{D} + \boldsymbol{L})^{-1} \left[\boldsymbol{E}^{(0)} - \boldsymbol{U}\widetilde{\boldsymbol{E}}^{k}\right]. \tag{A5}$$

By substituting the matrices $\boldsymbol{D}$, $\boldsymbol{L}$ and $\boldsymbol{U}$ for three subdomains and calculating the inverse of $(\boldsymbol{D} + \boldsymbol{L})$, we obtain:

$$\begin{bmatrix} \boldsymbol{E}^{(1)} \\ \boldsymbol{E}^{(2)} \\ \boldsymbol{E}^{(3)} \end{bmatrix}^{k+1} = \begin{bmatrix} \boldsymbol{A}_{11}^{-1} & \boldsymbol{0} & \boldsymbol{0} \\ -\boldsymbol{A}_{22}^{-1}\boldsymbol{A}_{21}\boldsymbol{A}_{11}^{-1} & \boldsymbol{A}_{22}^{-1} & \boldsymbol{0} \\ -\boldsymbol{A}_{31}^{-1} & -\boldsymbol{A}_{33}^{-1}\boldsymbol{A}_{32}\boldsymbol{A}_{22}^{-1} & \boldsymbol{A}_{33}^{-1} \end{bmatrix} \begin{bmatrix} \boldsymbol{R}_1 \\ \boldsymbol{R}_2 \\ \boldsymbol{R}_3 \end{bmatrix}, \tag{A6}$$

where

$$\boldsymbol{A}_{31}^{-1} = \boldsymbol{A}_{33}^{-1}\boldsymbol{A}_{31}\boldsymbol{A}_{11}^{-1} - \boldsymbol{A}_{33}^{-1}\boldsymbol{A}_{32}\boldsymbol{A}_{22}^{-1}\boldsymbol{A}_{21}\boldsymbol{A}_{11}^{-1}, \tag{A7}$$

and the terms $\boldsymbol{R}_i$ denote the ith row of the second term in the right-hand side of eq. (A5) written as

$$\begin{bmatrix} \boldsymbol{R}_1 \\ \boldsymbol{R}_2 \\ \boldsymbol{R}_3 \end{bmatrix} = \begin{bmatrix} \boldsymbol{E}^{(1,0)} - \boldsymbol{A}_{12}\boldsymbol{E}^{(2),k} - \boldsymbol{A}_{13}\boldsymbol{E}^{(3),k} \\ \boldsymbol{E}^{(2,0)} - \boldsymbol{A}_{23}\boldsymbol{E}^{(3),k} \\ \boldsymbol{E}^{(3,0)} \end{bmatrix}. \tag{A8}$$

By multiplying the matrix on the right-hand side of equation (A.6), we obtain the following equations:

$$\boldsymbol{E}^{(1),k+1} = \boldsymbol{A}_{11}^{-1}\boldsymbol{R}_1, \tag{A9}$$

$$\boldsymbol{E}^{(2),k+1} = \boldsymbol{A}_{22}^{-1}\left[\boldsymbol{R}_2 - \boldsymbol{A}_{21}\boldsymbol{A}_{11}^{-1}\boldsymbol{R}_1\right], \tag{A10}$$

$$\boldsymbol{E}^{(3),k+1} = \boldsymbol{A}_{33}^{-1}\left[\boldsymbol{R}_3 - \boldsymbol{A}_{32}\boldsymbol{A}_{22}^{-1}\left(\boldsymbol{R}_2 - \boldsymbol{A}_{21}\boldsymbol{A}_{11}^{-1}\boldsymbol{R}_1\right) - \boldsymbol{A}_{31}\boldsymbol{A}_{11}^{-1}\boldsymbol{R}_1\right]. \tag{A11}$$

Note that the term $\boldsymbol{A}_{11}^{-1}\boldsymbol{R}_1$ in the second right-hand side term of eqs (A10) and the third right-hand side term of (A11) can be substituted by $\boldsymbol{E}^{(1),k+1}$ from eq. (A9). Also, the term $\boldsymbol{A}_{22}^{-1}\left(\boldsymbol{R}_2 - \boldsymbol{A}_{21}\boldsymbol{A}_{11}^{-1}\boldsymbol{R}_1\right)$ in the second right-hand side term of eq. (A11) can be substituted by $\boldsymbol{E}^{(2),k+1}$ from eq. (A10). With substitutions on these terms, eqs (A9)–(A11) can be expressed as:

$$\boldsymbol{E}^{(1),k+1} = \boldsymbol{A}_{11}^{-1}\boldsymbol{R}_1, \tag{A12}$$

$$\boldsymbol{E}^{(2),k+1} = \boldsymbol{A}_{22}^{-1}\left[\boldsymbol{R}_2 - \boldsymbol{A}_{21}\boldsymbol{E}^{(1),k+1}\right], \tag{A13}$$

$$\boldsymbol{E}^{(3),k+1} = \boldsymbol{A}_{33}^{-1}\left[\boldsymbol{R}_3 - \boldsymbol{A}_{32}\boldsymbol{E}^{(2),k+1} - \boldsymbol{A}_{31}\boldsymbol{E}^{(1),k+1}\right], \tag{A14}$$

where the terms $\boldsymbol{A}_{ii}^{-1}$ are the block matrices that indicate the process of solving a linear system of equations in the ith subdomain. It can be observed from eqs (A12)–(A14) that, in general, there are recurrences of the term $\boldsymbol{E}^{(i),k+1}$ in all of the equations in the jth subdomain for $j > i$. This implies the results of the fixed-point eq. (A5) can be obtained by sequentially solving the linear system of equations in each subdomain and updating the right-hand side in the equations for the next subdomain using the most recent solutions.

APPENDIX B: VERIFICATION OF THE CONVENTIONAL IE CODE

To verify the accuracy of our conventional 3-D IE code, we compare our numerical results to those obtained with a semi-analytical 1-D solver (Shahriari *et al.* 2018) and a 3-D finite-volume solver (Hou *et al.* 2006). Following Jahani *et al.* (2023), we consider an LWD simulation across a layered anisotropic medium with a drilling angle of 80° as illustrated in Fig. B1. The tool consists of a tri-axial transmitter and receiver with a frequency of 12 kHz and a receiver spacing of 7.62 m. We use a moving forward modelling window with a size of 48.64 × 48.64 × 48.64 m^3. This window is discretized into 128 × 128 × 128 grid blocks and a cell size of 0.38 × 0.38 × 0.38 m^3. We set a constant background conductivity of 0.1118 S m^{-1}.

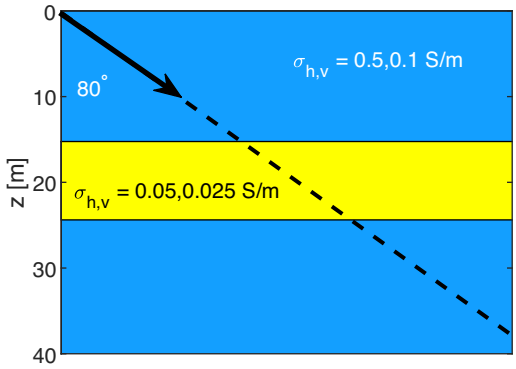

Figure B1. Sketch of logging while drilling across an anisotropic layered medium.

Fig. B2 shows the co-axial and co-planar components of the magnetic fields obtained using different numerical methods. We do not include the Y co-planar components of the magnetic fields because the values are zero. Overall, the results obtained from our IE-code show a good agreement with the 1-D semi-analytical and 3-D finite-volume results. The average absolute difference of all components calculated using our IE code is less than one per cent compared to the 1-D semi-analytical result.

APPENDIX C: CONDUCTIVITY TENSOR TRANSFORMATION FOR TRANSVERSELY ANISOTROPIC FORMATION

The tensor structure of electrical conductivity $\boldsymbol{\sigma}$ for anisotropic media is generally expressed as (Zhdanov 2009)

$$\boldsymbol{\sigma} = \begin{bmatrix} \sigma_{xx} & \sigma_{xy} & \sigma_{xz} \\ \sigma_{yx} & \sigma_{yy} & \sigma_{yz} \\ \sigma_{zx} & \sigma_{zy} & \sigma_{zz} \end{bmatrix}, \tag{C1}$$

with an off-diagonal symmetry $\sigma_{ij} = \sigma_{ji}$. For a vertical transverse isotropic medium with the z-axis as the vertical axis, the conductivity tensor is written as (Gao 2006; Jakobsen & Tveit 2018)

$$\boldsymbol{\sigma} = \begin{bmatrix} \sigma_h & 0 & 0 \\ 0 & \sigma_h & 0 \\ 0 & 0 & \sigma_v \end{bmatrix}, \tag{C2}$$

where σ_h and σ_v are the conductivity in the horizontal and vertical directions, respectively. In the case where the angle between the formation layering and the drilling trajectory is not 90°, it is necessary to rotate the conductivity tensor from the formation coordinate system to the induction tool coordinate system. For a transversely isotropic formation, the explicit expressions of the rotated conductivity tensor are as follows (Gao 2006)

$$\begin{aligned} \sigma'_{xx} &= \sigma_h + (\sigma_v - \sigma_h)\sin^2\theta\cos^2\phi, \\ \sigma'_{xy} &= (\sigma_v - \sigma_h)\sin^2\theta\sin\phi\cos\phi, \\ \sigma'_{xz} &= (\sigma_v - \sigma_h)\sin\theta\cos\theta\cos\phi, \\ \sigma'_{yy} &= \sigma_h + (\sigma_v - \sigma_h)\sin^2\theta\sin^2\phi, \\ \sigma'_{yz} &= (\sigma_v - \sigma_h)\sin\theta\cos\theta\sin\phi, \end{aligned} \tag{C3}$$

and

$$\sigma'_{zz} = \sigma_v - (\sigma_v - \sigma_h)\sin^2\theta,$$

where θ and ϕ are the z-axis rotation and y-axis rotation angles from the formation coordinate system to the induction tool coordinate system, respectively. The resulting conductivity tensor has non-zero off-diagonal components and our method can deal with this complication without making any other changes in the implementation.

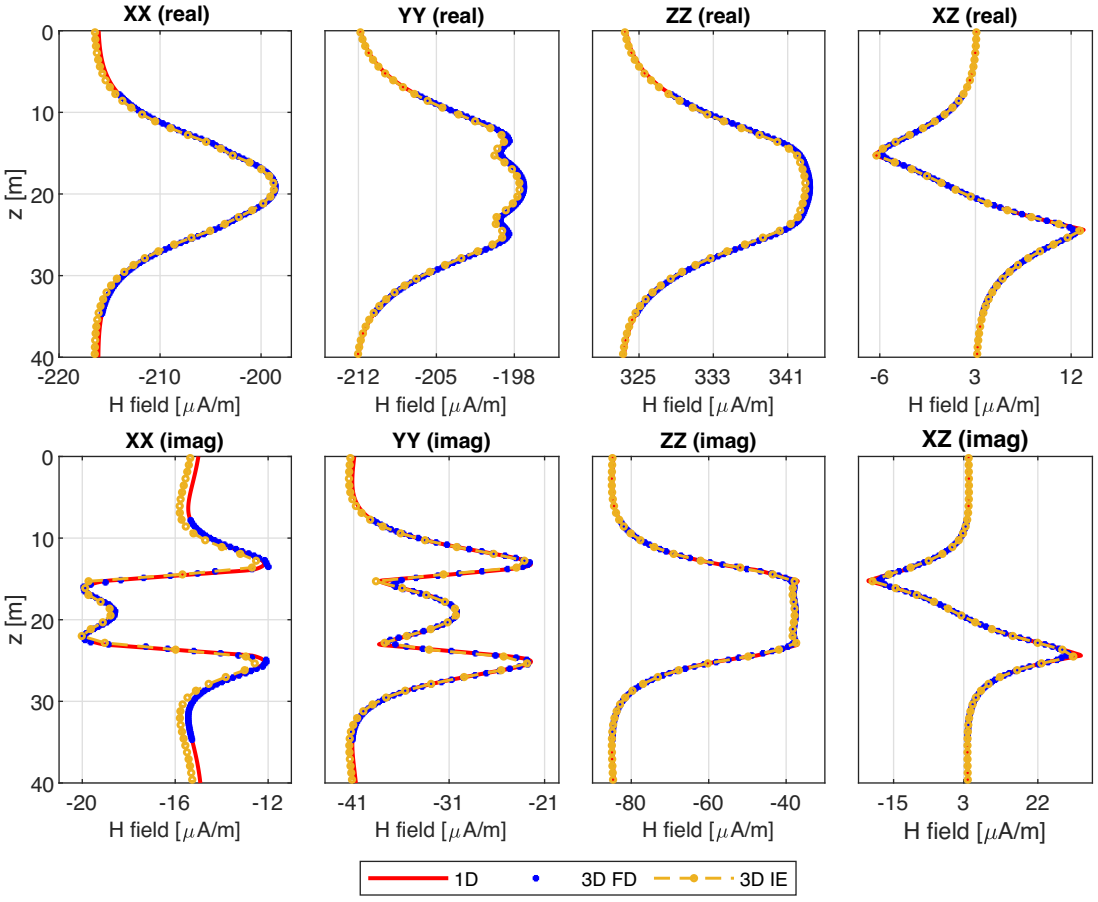

Figure B2. Comparison of the calculated magnetic field couplings with different numerical methods.